Faulting and hydration of the upper crust of the SW Okinawa Trough during continental rifting: Evidence from seafloor compliance inversion

Ban-Yuan Kuo, Wayne C. Crawford, Spahr C. Webb, Ching-Ren Lin, Tai-Chieh Yu, Liwen Chen

AGU PUBLICATIONS

Geophysical Research Letters

RESEARCH LETTER
10.1002/2015GL064050

Key Points:
- Seafloor compliance data are inverted for Okinawa Trough crustal structure
- V_S decreases and V_P/V_S increases with distance from Taiwan
- Faulting and hydration of the upper crust increase as rifting grows

Supporting Information:
- Supporting Information S1

Correspondence to:
B.-Y. Kuo,
byk@earth.sinica.edu.tw

Citation:
Kuo, B.-Y., W. C. Crawford, S. C. Webb, C.-R. Lin, T.-C. Yu, and L. Chen (2015), Faulting and hydration of the upper crust of the SW Okinawa Trough during continental rifting: Evidence from seafloor compliance inversion, *Geophys. Res. Lett.*, *42*, 4809–4815, doi:10.1002/2015GL064050.

Received 31 MAR 2015
Accepted 29 MAY 2015
Accepted article online 2 JUN 2015
Published online 23 JUN 2015

Faulting and hydration of the upper crust of the SW Okinawa Trough during continental rifting: Evidence from seafloor compliance inversion

Ban-Yuan Kuo[1], Wayne C. Crawford[2], Spahr C. Webb[3], Ching-Ren Lin[1], Tai-Chieh Yu[1], and Liwen Chen[4]

[1]Institute of Earth Sciences, Academia Sinica, Taipei, Taiwan, [2]Institut de Physique du Globe de Paris, Paris, France, [3]Lamont-Doherty Earth Observatory, Palisades, New York, USA, [4]Institute of Oceanography, National Taiwan University, Taipei, Taiwan

Abstract The elastic response of seafloor to ocean gravity wave loading, or seafloor compliance, provides a constraint on the elastic properties of the crust. We measured seafloor compliance at three ocean bottom seismometer (OBS) sites around Taiwan—two in the southwestern (SW) Okinawa Trough and one on the Ryukyu arc—and performed inversion for crustal structures beneath them. Models best fitting the data demonstrate a decrease in upper crustal shear velocity and an increase in the compressional/shear velocity ratio from the arc site to the trough sites with increasing amount of back-arc extension. This variation suggests that the upper continental crust is highly faulted and hydrated during rifting of the Eurasian lithosphere.

1. Introduction

Rifting of continental and oceanic lithosphere is accompanied by stretching of the lithosphere and faulting of the brittle upper crust [*Buck*, 1991; *Huismans and Beaumont*, 2011]. The Okinawa Trough (OT), a continental back-arc basin, was formed by rifting of the present-day Ryukyu island arc from the Eurasian continental margin as a result of subduction of the Philippine Sea Plate (Figure 1). Seismic surveys and seafloor morphology indicate that the Okinawa Trough tapers westward in the last few hundred kilometers and terminates beneath the Yilan Plain in NE Taiwan [*Sibuet et al.*, 1998]. The retreat of the Ryukyu arc decelerates drastically where the trench meets the Eurasian continent [*Nakamura*, 2004]. The slowing of the trench retreat and closing of the OT may be mechanically governed by the locking of the Philippine Sea Plate slab onto the Eurasian lithosphere through oblique subduction [*Ko et al.*, 2012]. How the crust of the OT has accommodated this tectonic constraint has not been investigated. In the past, active-source OBS experiments have been conducted in this region to constrain mainly *P* wave velocity (V_P) structures [e.g., *Wang et al.*, 2004; *McIntosh et al.*, 2005; *Klingelhoefer et al.*, 2009]. *S* wave velocities (V_S) are more sensitive to faulting and the subsequent alternation of the crust, but models of V_s along the OT have rarely been reported.

Several portable ocean bottom seismometers (OBSs) have been deployed in the southwest OT since 2006 [*Lin et al.*, 2009], offering a sporadic yet unique glimpse into the crust and mantle there [e.g., *Kuo et al.*, 2012]. In addition to these campaign-mode observations, a permanent seafloor observatory was installed on the westernmost extension of the Ryukyu arc, or the Yilan ridge [*Hsu*, 2013], by the Central Weather Bureau (CWB) of Taiwan, from which data are retrieved in real time since late 2011. In this study, we analyze seafloor compliance functions from two portable broadband OBSs, S002 and S005, and from the CWB seafloor observatory EOS1 to constrain V_S structures of the crust beneath these three sites (Figure 1). S002 and S005, each deployed for 10 months, are situated in the back-arc basin at different distances from Taiwan, whereas EOS1, with over 2 years of data, provides a reference of nonrifting continental crust.

2. Data

The details of the instruments and operations of these OBS sites can be found in *Lin et al.* [2009] and *Hsiao et al.* [2014], and the data selection and analysis procedure were fully documented in *Kuo et al.* [2014]. We calibrated the amplification factor of the pressure gauge using Rayleigh waves [*Zha et al.*, 2014].

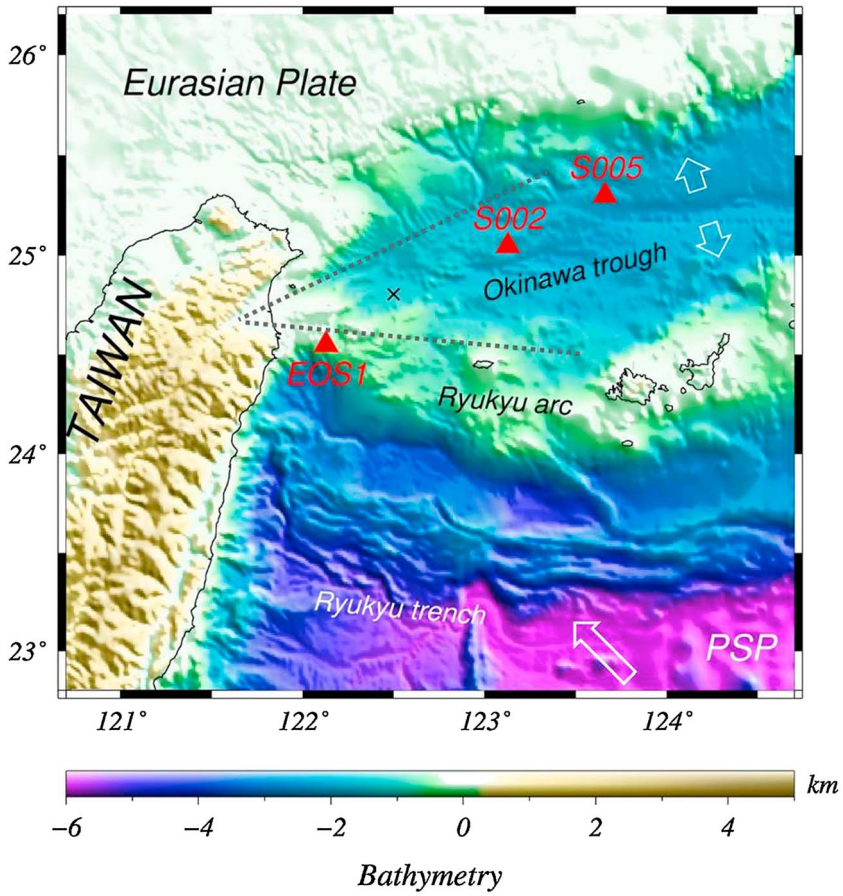

Figure 1. Bathymetry map showing tectonic elements of the Okinawa Trough-Ryukyu subduction system and the locations of EOS1, S002, and S005, the 3 broadband OBSs (red triangle) used in the study. Filled arrow indicates oblique subduction of the Philippine Sea Plate (PSP). Open arrows indicate relative motion of the continental back-arc extension along the Okinawa Trough. The 2 grey dotted lines imply the growth of rifting away from Taiwan. The cross marks the location of the ODP1202 site.

The compliance function measures the ratio of the vertical displacement of seafloor to the pressure induced by ocean waves in the infragravity wave frequency band and provides information about the sediment and crustal structure beneath an OBS [*Crawford et al.*, 1998]. The compliance function η_{dp} is defined in frequency domain (f) as

$$\eta_{dp}(f) = \gamma_{dp}(f) \cdot \sqrt{\frac{G_{dd}(f)}{G_{pp}(f)}} \tag{1}$$

where G_{dd} and G_{pp} are autospectra of vertical displacement and pressure, respectively, and γ_{dp} is the coherence between vertical displacement and pressure defined as

$$\gamma_{dp}(f) = \frac{G_{dp}(f)}{\sqrt{G_{dd}(f) \cdot G_{pp}(f)}} \tag{2}$$

with G_{dp} being cross spectrum between displacement and pressure (Figure S1 in the supporting information). Formal error is calculated from equation (4) of *Crawford et al.* [1991]. The error is 1–6% of the compliance value for S002 and S005 and around 1% at low frequencies and much smaller than 1% at middle frequencies for EOS1 due to its high coherence and large number of data windows (~2000) [*Kuo et al.*, 2014]. In the inversion below, we set the minimum value of error at 1%. *Kuo et al.* [2014] demonstrated that the bottom motions forced by the infragravity waves can be isolated and removed from these OBS data to recover seismic signals. In this study, we

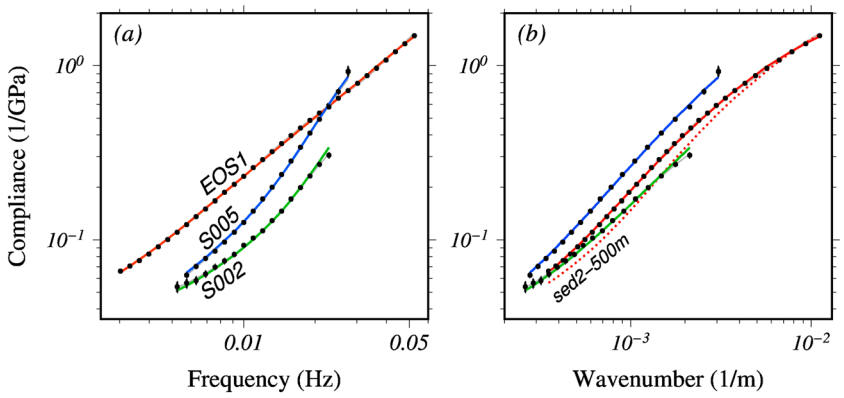

Figure 2. The compliance measurements (dots) with error (vertical bar) vs. (a) frequency and (b) wave number for the 3 OBSs as labeled. The grey lines are predicted values from the five-layer model. Three color lines, with red for EOS1, green for S002, and blue for S005, are predicted values from the smooth model. Most part of the grey and color lines overlap for each OBS. Plotting compliance against wave number in (b) neutralizes the influence of water depth, rendering a direct comparison for sedimentary and crustal structures. Red dotted line denotes the compliance calculated from the best EOS1 model with layer 2 replaced by that of the S002 (see Discussion).

utilize the compliance as a signal. The observed compliance functions for EOS1, S002, and S005 are shown in Figure 2. The compliance is multiplied by wave number (k) to produce a constant value for a structure with uniform elastic properties.

While seafloor motion is driven by water pressure, the OBS signal can be perturbed by the gravitational attraction of the sea surface mass perturbation, especially at low frequencies and shallow water depths [*Crawford et al.*, 1998]. For EOS1 where water depth is only 300 m, the gravitational attraction signal can reach one tenth of the observed displacement at periods of ~200 s (Figure S2 in the supporting information). With greater water depths at S002 (1740 m) and S005 (1900 m), this effect is shifted toward lower frequencies. We corrected the gravitational attraction effect from the observed compliance for each OBS.

We identified noise in the vertical data that is highly coherent with the horizontal data for S002 and S005 at frequencies < 0.01 Hz and removed it using the same technique as that for removing the infragravity wave noise [*Crawford and Webb*, 2000]. This noise comes from tilting of the sensor under seafloor currents, which is exacerbated by a soft seabed and imperfect alignment of the vertical channel with the gravitational field. Removing the tilt noise improves the coherence, reduces the error, and slightly increases the amplitude of the compliance function (Figures S3 and S4 in the supporting information).

3. Five-Layer Model

The measured compliance is resampled into 32, 17, and 18 data points equally spaced in log frequency domain for EOS1, S002, and S005, respectively, for the inversion. To invert for crustal structure from the compliance measurements, we started with a simple model in which we divided sediments into two layers and crust into three layers. Sediment thickness h was estimated in *Kuo et al.* [2014], and the two layers within the sediment are assumed to be 200 m and $h - 200$ m thick, respectively. The first crustal layer (crust 1) is 1 km thick, overlying a 2 km thick second layer (crust 2) on top of a half-space. We systematically search for the density (ρ), V_P, and V_S of the sediment and crust that best fit the observed compliance data.

The compliance is more sensitive to V_S than to V_P and ρ, especially for structures with high V_P/V_S or equivalently high Poisson's ratio [*Crawford et al.*, 1999]. In previous compliance studies, V_P and ρ structures of the crust were often determined by active-source seismic modeling for the same OBS and thus were fixed in the inversion. In this study, such independent, in situ constraints for each OBS are not available. The V_P models from *Wang et al.* [2004] are the closest but are still 50 km away from EOS1. Rather than fixing these parameters, we imposed maximum V_P values of 2, 4, 5, 6, and 6.5 km/s in layers 1–5, respectively. These maximum values were chosen by examining the velocity of the shallow, unconsolidated sediment documented in the ODP 1202 site report [*Salisbury et al.*, 2002], the velocity of

Table 1. Summary of the Statistical Performance of the Best Fit Model for Each OBS[a]

	χ^2	RMS Misfit (10^{-3} 1/GPa)	V.R. (%)	nfr	$\Sigma 1/\sigma^2$ (10^6 GPa^2)
EOS1-five layers	0.96	1.758	99.99	32	9.939
EOS1-smooth	1.08	1.865	99.99		
S002-five layers	0.26	1.124	99.95	17	3.516
S002-smooth	0.62	1.738	99.88		
S005-five layers	0.32	1.191	99.99	18	4.010
S005-smooth	1.00	2.117	99.98		

[a]V.R. (%): variance reduction in percentage; nfr: number of data in frequency; RMS misfit: root-mean-square misfit weighted by error σ; $\Sigma 1/\sigma^2$: the sum of the inverse of error, the weighting factor in calculating misfit.

consolidated marine sediment [*Shillington et al.*, 2008], and crustal models in this region [*Wang et al.*, 2004; *Klingelhoefer et al.*, 2009]. The respective maximum V_S is given as V_P/1.7 (see below). The minimum V_S, always in sediment layers, is set at 0.4 km/s.

Using the forward calculation technique formulated in *Crawford et al.* [1991], a grid search with progressive decreasing of grid interval was performed. The grid search starts with a wide model range and a grid interval of 0.2 km/s for V_P and V_S and 0.2 g/cm^3 for ρ. A best fit model is achieved when error-weighted misfit of compliance reaches a minimum among all trials. The second run starts with the best fit model from the first run and a search range narrowed and search interval halved (Figure S5 in the supporting information). A few conditions were implemented to regularize the grid search. All model parameters are allowed only to increase with depth as the compliance data do not display obvious peaks that suggest the presence of a low shear strength zone, and V_P/V_S is set to be >1.7 because porosity, faulting, hydration, and melting only increase the velocity ratio from the value for a Poisson solid. In the bottom half-space layer, V_P is fixed as $V_P = V_S \times 1.73$ and ρ is fixed at 2.8 g/cm^3 to speed up the search. There are a total of 13 free parameters to be determined, and two or three runs can lead to a final model with a variance reduction $>99.5\%$. Table 1 summarizes the statistical performance of the best fit model for each OBS.

Figure 3a shows the best fit five-layer models of V_S. The predictions in compliance from these models are shown with the data in Figure 2. The first-order feature among the three models is the decreasing V_S in the crustal layers from EOS1 to S002 and to S005. The variation is most significant in the shallow

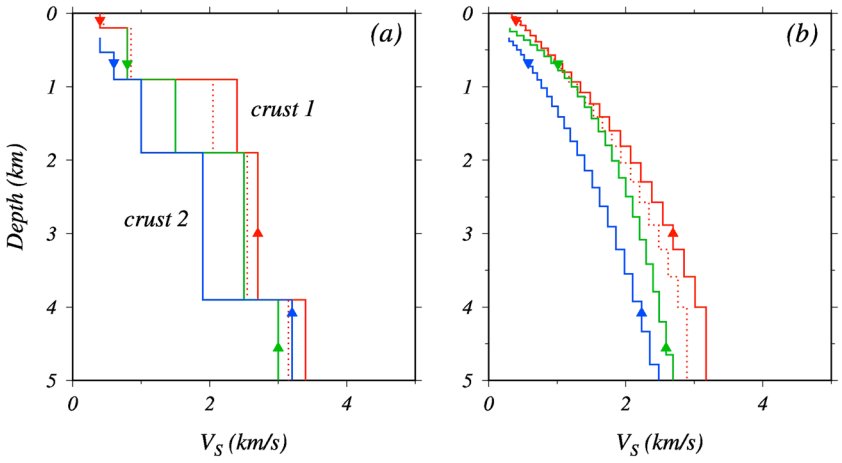

Figure 3. (a) V_S of the five-layer models determined from a grid search. EOS1 in red, S002 in green, and S005 in blue. Three models have different sediment thickness and they are plotted such that the depths to the basement for S002 and S005 match that for EOS1. Note the decrease in the top layer of the crust, or crust 1, from EOS1, S002, to S005. Triangle and inverse triangles mark the depths of maximum sensitivity for the lowest and highest frequencies of the data, respectively, an indication of the range of resolution model can provide. Dotted lines are models for EOS1 without the data at frequencies beyond the maximum frequency for S005, showing the same trend of decreasing V_S from EOS1 to S005. (b) The smooth models of V_S from the Occam's inversion with ρ and V_P inherited and slightly smoothed from the five-layer model in (a). The variation in shallow crust across the 3 OBSs is highly suppressed while the trend of decreasing V_S from EOS1 to S005 remains in a thicker crustal section. Dotted lines are the counterpart of that in (a) for EOS1.

crust or "crust 1." As a rule, the compliance at a particular frequency is most sensitive to the V_S at the depth corresponding to one sixth of the wavelength of the infragravity wave at that frequency [*Crawford et al*., 1999]. Crust 1 of each model is in the center of the corresponding sensitivity depth range. We performed a series of grid searches with different thickness for crust 1, finding that the relative amplitudes of V_S in this layer among the three sites are preserved until it is thicker than 5 km (Figure S5 in the supporting information).

4. Smooth Model

While the five-layer model explains the data satisfactorily, its oversimplified layering may introduce artificial discontinuities. The alternative approach is to fit the data with a structure as smooth as possible. We employ the Occam's inversion adopted by *Crawford et al*. [1991, 1999] to calculate the smooth model. We discretize the sediment and crust into thin layers with a 50 m thick top layer, layer thicknesses increasing by a factor of 1.1 with each deeper layer to compensate for the decay in the influence of the medium with depth. The starting model for the Occam's inversion is the slightly smoothed five-layer model, but only V_S is inverted for in the Occam's inversion. The performance of the inversion degrades with decreasing depth of the half-space. We adopted the half-space as shallow as possible while retained high data fitting: 4 km for EOS1 and 8 km for both S002 and S005. The inversion has 24, 30, and 30 unknowns, corresponding to the numbers of layers, for EOS1, S002, and S005, respectively. While these numbers are comparable to or exceed the numbers of data, the true degree of freedom for each model is necessarily suppressed by the requirement of minimum curvature in the Occam's inversion.

Figure 3b exhibits the smooth models for EOS1, S002, and S005. With all the discontinuities eliminated (Figure S6 in the supporting information), the smooth models explain the data equally well as the five-layer model (Table 1). Because the Occam's inversion iterates to locate the minimum curvature solution that fits the data to within the given error, it may not surpass the performance of the grid search. Without the sediment-crust discontinuity, the trend of increasing V_S from EOS1 to S005 is manifested in a distributed depth range.

5. Interpretation

The five-layer and the smooth models represent results from two end-member parameterizations that yield nearly equal fit to the data (Table 1). Both show the general pattern of V_S in the crust decreasing from EOS1 to S005. Nonetheless, our interpretation is focused on the 1 km thick crust 1 of the five-layer model, which is likely to extract the properties of the shallow crust while preserving the possibility of the presence of the sediment-crust discontinuity. We performed a resolvability test in which velocities of each of the five layers are perturbed around the best fit values and inspected how data fitting degrades (Figure 4). A tight peak in variance reduction distribution indicates a good constraint of the best fit model, whereas a plateau implies a poor one. Separate narrow peaks for the three OBSs represent distinguishable solutions among them. Figure 4c demonstrates that the V_S of crust 1 is highly distinguishable between EOS1 and S005 and between S002 and S005 and moderately distinguishable between EOS1 and S002. We propose that the trend of decreasing V_S in the shallow crust from EOS1 to S002 and then to S005 is statistically acceptable or significant. We interpret this trend as indicative of increasing degree of faulting of the brittle crust.

During rifting, normal faulting forms in the brittle upper crust to accommodate the stretching of the entire lithosphere [*Buck*, 1991]. As a rift widens, new faults develop, fault blocks rotate, and slips along existing faults increase as the crust stretches and thins [*Huismans and Beaumont*, 2011]. Because the OT closes toward Taiwan, it is likely that S005 samples the crust stretched and faulted more significantly than S002 where rifting is immature, whereas EOS1 characterizes the drift-away continental block that has not undergone rifting. Half-graben structures with normal faults cutting into the crust were found pervasive in reflection profiles east of S005 [e.g., *Park et al*., 1998]. Recent seismic imaging studies revealed that little faults have developed on the Yilan ridge, where EOS1 is installed [*Hsu*, 2013]. However, in the tapering zone of the OT, where S002 is located, imaging faults in the crust become difficult because sediment thickens as the Asian continent is approached [*Hsu*, 2013].

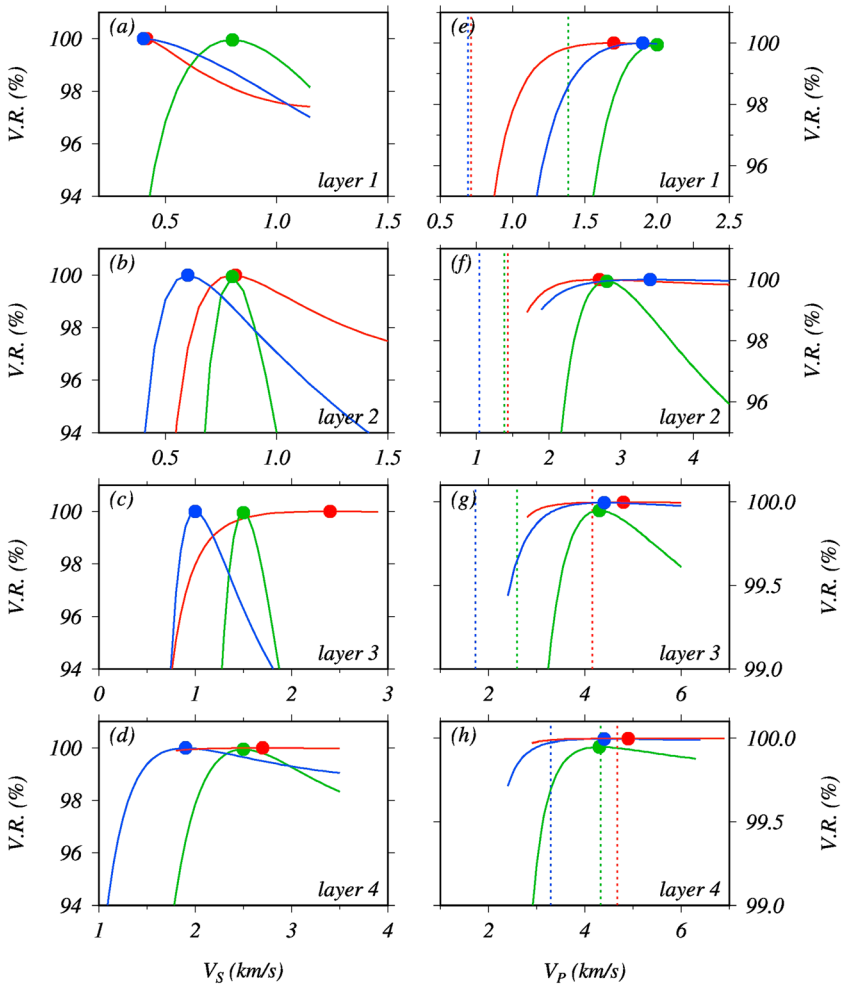

Figure 4. A resolvability test with variation reduction vs. V_S (a–d) and V_P (e–h) for layers 1–4 of the five-layer model. Color code for OBS is the same as in Figure 3. The variance reduction (curve) drops from the maximum (dot) when the velocity of each layer is perturbed from the best fit value. Panel c shows that the differences in shallow curst among the 3 sites are moderately or well resolved. For V_P, vertical dotted lines represent 1.73 × the best fit V_S. Panel g shows that the best fit V_P's are distinct from and higher than their corresponding Poisson solid properties for S002 and S005, but not for EOS1. Note the change in variance reduction is much smaller for V_P than for V_S.

6. Discussion

The high compliance for EOS1 compared with S002 and S005 in Figure 2a seemingly contradicts the expectation that higher V_S generates lower compliance. Plotting compliance versus the wave number of the infragravity waves (Figure 2b) equalizes the difference in water depth, rendering a direct comparison in sedimentary and crustal structures. However, the compliance for EOS1 in Figure 2b is still higher than that for S002. This is because the sediment at EOS1 is thicker than that at S002, i.e., 900 m versus 700 m. In our five-layer model configuration, layer 2 is 700 m thick in EOS1 and 500 m thick in S002. We replaced the layer 2 of EOS1 with that of S002 (including all parameters) and calculated the theoretical compliance, which is now below that of S002, in agreement with the expectation.

We find that V_P/V_S in crust 1 increases from 2 beneath EOS1 to 2.9 beneath S002 and 4.4 beneath S005 (Figure S7 in the supporting information). Because V_P is a low-sensitivity parameter in the inversion [e.g., *Zha et al.*, 2014], we ran a resolvability test on V_P to check whether this observation is fortuitous. In this layer, V_P is capped at 5 km/s. Figure 4g shows that, even though the variance reduction drops only incrementally for lower velocities, the V_P's in crust 1 beneath S002 and S005 are distinguishable from and higher than the corresponding Poisson solid values, i.e., 1.73 times the best fit V_S. On the contrary, the V_P in crust 1

beneath EOS1 could be smaller than its Poisson solid value, rendering a possibility of lower V_P/V_S than that appears in the best fit model. This corroborates the increasing trend in V_P/V_S from EOS1 to S005.

The presence of faults facilitates water infiltration and hydration of the crust along them, which further lowers the shear strength of the crust. As for the case of oceanic crust and mantle [e.g., *Ranero and Sallarès*, 2004; *Chou et al*., 2009], the anticorrelation between V_P/V_S and V_S is a sign of hydration and/or melting of the material. The increase in V_P/V_S and decrease in V_S from Taiwan eastward into the OT suggest increasing hydration of the shallow continental crust while rifting grows.

The shallow EOS1 site allows compliance to be estimated at significantly higher frequencies than at the other two sites. We tested whether this high-frequency data are necessary in order to draw the inference above, by removing the EOS1 compliance values at frequencies higher than the high-frequency limit at S005 and rerunning the inversion. The resulting model had higher V_S in the sediment and lower V_S in the crust (Figure 3), but the trend of increasing crust 1 V_S persists. In the smooth model calculated using these "muted data," V_S is reduced accordingly and the general trend holds. In summary, the most prominent pattern of this study is consistent with a scenario in which the elastic properties of the shallow crust of the OT are controlled by rifting-induced faulting and hydration.

Acknowledgments

We thank critical comments from two reviewers. The portable OBSs were cobuilt in WHOI OBS laboratory under a collaborative project with John Collins and Ken Peal. These data can be requested from IES data management center at http://dmc.earth.sinica.edu.tw or from B.Y.K. on a collaboration basis. The EOS1 data can be requested from the CWB. The research was supported by the Ministry of Science and Technology (MOST) of Taiwan, Republic of China, under grant MOST-102-2116-M-001-026. L.C. is supported by MOST 104-3113-M-002-004.

The Editor thanks two anonymous reviewers for their assistance in evaluating this paper.

References

Buck, W. R. (1991), Modes of continental lithospheric extension, *J. Geophys. Res.*, *96*, 20,161–20,178, doi:10.1029/91JB01485.

Chou, H. C., B. Y. Kuo, L. Y. Chiao, D. Zhao, and S. H. Hung (2009), Tomography of the western Ryukyu subduction zone and the serpentinization of the fore-arc mantle, *J. Geophys. Res.*, *114*, B12301, doi:10.1029/2008JB006192.

Crawford, W. C., and S. C. Webb (2000), Identifying and removing tilt noise from low-frequency (<0.1 Hz) seafloor vertical seismic data, *Bull. Seismol. Soc. Am.*, *90*, 952–963.

Crawford, W. C., S. C. Webb, and J. A. Hildebrand (1991), Seafloor compliance observed by long-period pressure and displacement measurements, *J. Geophys. Res.*, *96*, 16,151–16,160, doi:10.1029/91JB01577.

Crawford, W. C., S. C. Webb, and J. A. Hildebrand (1998), Estimating shear velocities in the oceanic crust from compliance measurements by two-dimensional finite difference modeling, *J. Geophys. Res.*, *103*, 9895–9961, doi:10.1029/97JB03532.

Crawford, W. C., S. C. Webb, and J. A. Hildebrand (1999), Constraints on melt in the lower crust and Moho at the East Pacific Rise, 9 48′N, using seafloor compliance measurements, *J. Geophys. Res.*, *104*, 2923–2939, doi:10.1029/1998JB900087.

Hsiao, N. C., T. W. Lin, S. K. Hsu, K. W. Kuo, T. C. Shin, and P. L. Leu (2014), Improvement of earthquake locations with the Marine Cable Hosted Observatory (MACHO) offshore NE Taiwan, *Mar. Geophys. Res.*, *35*, 327–336, doi:10.1007/s11001-013-9207-3.

Hsu, H. H. (2013), Seismic imaging of sediment dispersal systems: Southwest and northeast Taiwan perspectives [in Chinese], PhD thesis, 166 pp., Institute of Oceanography, National Taiwan Univ., Taipei.

Huismans, R., and C. Beaumont (2011), Depth-dependent extension, two-stage breakup and cratonic underplating at rifted margins, *Nature*, *473*, 74–78, doi:10.1038/nature09988.

Klingelhoefer, F., C. S. Lee, J. Y. Lin, and J. C. Sibuet (2009), Structure of the southernmost Okinawa Trough from reflection and wide-angle seismic data, *Tectonophysics*, *466*, 281–288, doi:10.1016/j.tecto.2007.11.031.

Ko, Y. T., B. Y. Kuo, K. L. Wang, S. C. Lin, and S. H. Hung (2012), The southwestern edge of the Ryukyu subduction zone: A high *Q* mantle wedge, *Earth Planet. Sci. Lett.*, *335–336*, 145–153, doi:10.1016/j.epsl.2012.04.041.

Kuo, B. Y., C. C. Wang, S. C. Lin, C. R. Lin, P. C. Chen, J. P. Jang, and H. K. Chang (2012), Shear-wave splitting at the edge of the Ryukyu subduction zone, *Earth Planet. Sci. Lett.*, *355–356*, 262–270, doi:10.1016/j.epsl.2012.08.005.

Kuo, B. Y., S. C. Webb, C. R. Ling, W. T. Liang, and N. C. Hsiao (2014), Removing infragravity-wave induced noise from OBSs data deployed offshore of Taiwan, *Bull. Seismol. Soc. Am.*, *104*, 1674–1684, doi:10.1785/0120130280.

Lin, C. R., B. Y. Kuo, W. T. Liang, W. C. Chi, Y. C. Huang, J. Collins, and C. Y. Wang (2009), Ambient noise and teleseismic signals recorded by ocean-bottom seismometers offshore eastern Taiwan, *Terr. Atmos. Ocean. Sci*, *21*, 743–755, doi:10.3319/TAO.2009.09.14.01(T).

McIntosh, K., Y. Nakamura, T. K. Wang, R. C. Shih, A. Chen, and C. S. Liu (2005), Crustal-scale seismic profiles across Taiwan and the western Philippine Sea, *Tectonophysics*, *401*, 23–54.

Nakamura, M. (2004), Crustal deformation in the central and southern Ryukyu arc estimated from GPS data, *Earth Planet. Sci. Lett.*, *217*, 389–398.

Park, J. O., H. Tokuyama, M. Shinohara, K. Sueyhiro, and A. Taira (1998), Seismic record of tectonic evolution and backarc rifting in the southern Ryukyu island arc system, *Tectonophysics*, *294*, 21–42.

Ranero, C. R., and V. Sallarès (2004), Geophysical evidence for hydration of the crust and mantle of the Nazca Plate during bending at the north Chile trench, *Geology*, *32*, 549–552, doi:10.1130/G20379.1.

Salisbury, M. H., et al. (2002), *Proceedings of the Ocean Drilling Program, Init. Rep*., vol. 195, Ocean Drilling Program, College Station, Tex., doi:10.2973//odp.proc.ir.195.2002.

Shillington, D. J., T. Minshull, C. Peirce, and J. M. O'Sullivan (2008), *P*- and *S*-wave velocities of consolidated sediments from a seafloor seismic survey in the North Celtic Sea Basin, offshore Ireland, *Geophys. Prospect.*, *56*, 197–211, doi:10.1111/j.1365-2478.2007.00669.x.

Sibuet, J. C., B. Deffontaines, S. K. Hsu, N. Thareau, J. P. Le Formal, C. S. Liu, and ACT party (1998), Okinawa trough backarc basin: Early tectonic and magmatic evolution, *J. Geophys. Res.*, *103*, 30,245–30,267.

Wang, T. K., S. F. Lin, C. S. Liu, and C. S. Wang (2004), Crustal structure of the southernmost Ryukyu subduction zone: OBS, MCS and gravity modeling, *Geophys. J. Int.*, *157*, 147–163.

Zha, Y., S. C. Webb, S. L. Nooner, and W. C. Crawford (2014), Spatial distribution and temporal evolution of crustal melt distribution beneath the East Pacific Rise at 9°–10°N inferred from 3-D seafloor compliance modeling, *J. Geophys. Res. Solid Earth*, *119*, 4517–4538, doi:10.1002/2014JB011131.